Quantifying Safety of Laser-Based Navigation

MATHIEU JOERGER, Senior Member, IEEE
University of Arizona, Tucson, AZ USA

BORIS PERVAN, Senior Member, IEEE
Illinois Institute of Technology, Chicago, IL USA

In this paper, a new safety risk evaluation method is developed, simulated, and tested for laser-based navigation algorithms using feature extraction (FE) and data association (DA). First, at FE, we establish a probabilistic measure of separation between features to quantify the sensor's ability to distinguish landmarks. Then, an innovation-based DA process is designed to evaluate the impact on integrity risk of incorrect associations, while considering all potential measurement permutations. The algorithm is analyzed and tested in a structured environment.

Manuscript received July 24, 2017; revised January 26, 2018; released for publication April 7, 2018. Date of publication June 25, 2018; date of current version February 7, 2019.

DOI. No. 10.1109/TAES.2018.2850381

Refereeing of this contribution was handled by Z. Zhu.

This work was supported in part by the Federal Aviation Administration, and in part by the National Science Foundation under FAA Grant #14-G-018, NSF award #1637899.

Authors' addresses: M. Joerger is with the University of Arizona, Tucson, AZ 85721 USA, E-mail: (joerger@email.arizona.edu); B. Pervan is with the Illinois Institute of Technology, Chicago, IL 60616USA, E-mail: (pervan@iit.edu). *(Corresponding author: Mathieu Joerger.)*

0018-9251 © 2018 IEEE

I. INTRODUCTION

This paper describes the design, analysis, and testing of a new integrity risk monitoring method for laser-based feature extraction (FE) and data association (DA). FE and DA are preestimator measurement processing functions that are implemented in laser-based navigation applications [1]–[15]. The methods developed in this paper provide the means to *quantify safety risks* involved with FE and DA, which is not fully addressed in the literature. This will help ensure navigation safety in life-critical applications, including in highly-automated vehicle (HAV) localization.

Currently, the most publicized efforts to demonstrate HAV safety are Waymo's (formerly Google's) and Tesla's approaches to have HAVs drive millions of miles with minimal human intervention. At this time, Waymo cars have autonomously travelled an impressive three million miles in urban areas [16]. Tesla's autopilot is reported to have driven more than 130 million miles—-on highways only—-before it caused a fatality in May 2016 [17], [18]. In parallel, the National Highway Traffic Safety Administration (NHTSA) reports about one fatality in traffic accidents per 100 million mile driven by human drivers in the U.S. [19], [20]. But, this number accounts for incidents on all roads, in all weather conditions, and for all vehicle ages and types. Thus, a purely experimental, complete proof that HAVs match the level of safety of human driving would require billions of miles driven [21]. This is assuming that no fatalities occur during that time, that no major HAV upgrade is performed, and that the testing environment is representative of all U.S. roads. Clearly, other methods must also be employed to ensure HAV safety.

As a complement to testing, this paper leverages prior analytical work carried out in civilian aviation navigation (as recently suggested in [22]), where safety is assessed in terms of integrity. Integrity is a top-level, quantifiable performance metric, which is sensor-independent and platform-independent. It can be used to set certifiable requirements on individual system components to achieve and prove an overall level of safety. Integrity is a measure of trust in sensor information: integrity risk is the probability of undetected sensor errors causing unacceptably large positioning uncertainty [23]. Loss of integrity can place the HAV in hazardous situations.

Several methods have been established to predict the integrity risk in Global Navigation Satellite Systems (GNSS)-based aviation applications, which are instrumental in ensuring the safety of pilots and crew [23]–[26]. Unfortunately, the same methods do not directly apply to HAVs, because ground vehicles operate under sky-obstructed areas where GNSS signals can be altered or blocked by buildings and trees.

HAVs require sensors in addition to GNSS, including laser scanners, cameras, or radars. This paper focuses on laser scanners because of their prevalence in HAVs, of their market availability, and of our prior experience. A raw laser scan is made of thousands of data points, each of which individually does not carry any useful information. Raw

Authorized licensed use limited to: to IEEExplore provided by University Libraries | Virginia Tech. Downloaded on August 17,2020 at 19:20:58 UTC from IEEE Xplore. Restrictions apply.

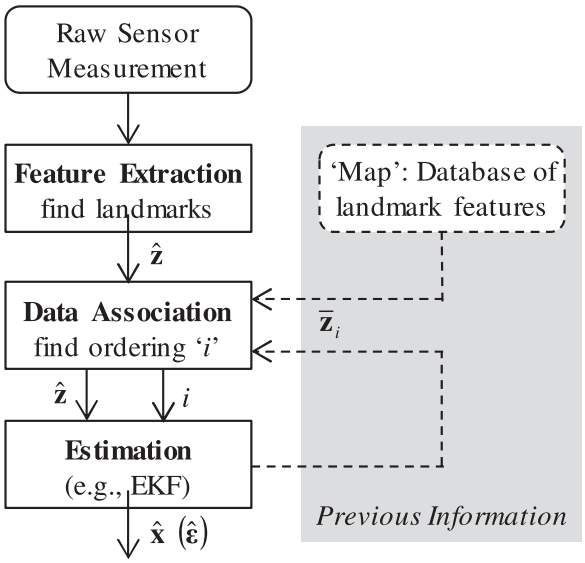

Fig. 1. Three step estimation process for laser or radar-based navigation.

measurements must be preprocessed before they can be used for navigation [8], [27]–[28]. A first class of algorithms establishes correlations between successive scans to estimate sensor changes in "pose" (i.e., position and orientation) [29]–[32]. These procedures can become inaccurate or cumbersome for HAVs moving over multiple time epochs. A second class of algorithms provides sensor localization by tracking recognizable, static features in the perceived environment.

Features can include, for example, lines or planes corresponding to building walls in two- or three-dimensional (2D or 3D) scans, respectively. Extracted feature parameters, such as current-time coordinates in a local East–North-Up navigation frame of the vector normal to line- or plane-features, are noted $\hat{\mathbf{z}}$ in Fig. 1. Features that can be exploited in this research not only include position and orientation, but also landmark size, surface color, reflectivity, roughness, or any other measurable characteristic. Previous knowledge of feature parameters (noted $\bar{\mathbf{z}}_i$ in Fig. 1) can be provided either from a landmark map or from past-time estimation in simultaneous localization and mapping (SLAM) [27], [28]. The resulting information can then be iteratively processed using sequential estimators (e.g., Extended Kalman filter or EKF), which is convenient in many practical applications [8], [27], [28]. The problems that FE and DA are addressing are the following [2], [5], [7], [8].

First, raw laser observations of landmarks do not come with a label or "name tag" like a GNSS satellite signal's pseudo random noise number, for example. Thus, FE aims at finding the few most consistently recognizable, viewpoint-invariant landmarks in the raw sensor data. The extracted features must not only be identifiable over repeated observations, but must also be distinguishable from one landmark to another. Features that are difficult to distinguish or "poorly separated" are easily found, but are likely to be incorrectly associated, which will impact integrity.

Second, lasers provide pose estimation by comparing current-time landmark feature measurements $\hat{\mathbf{z}}$ to prior knowledge of these features $\bar{\mathbf{z}}_i$ [27], [28]. $\bar{\mathbf{z}}_i$ assumes an ordering of landmarks designated by subscript i (there are many possible orderings). DA aims at assigning the landmark features $\hat{\mathbf{z}}$ to the corresponding feature parameters assumed in the estimation process, i.e., at finding the ordering of landmarks i in $\bar{\mathbf{z}}_i$ that matches the ordering of landmarks in $\hat{\mathbf{z}}$ over successive observations [4]. Incorrect association (IA) is a well-known problem that can lead to large navigation errors [33], thereby representing a threat to navigation integrity.

FE and DA can be challenging in the presence of sensor uncertainty. This is why many sophisticated algorithms have been devised [1]–[15]. But, how can we prove whether these FE and DA methods are safe for life-critical HAV navigation applications, and under what circumstances?

These research questions are mostly unexplored. The most relevant publications are found in literature on multitarget tracking. For example, in [1], an innovation-based nearest-neighbor DA criterion is introduced, which serves as basis in many practical implementations. Bar-Shalom *et al.* in [34] provides a detailed derivation of the probability of correct association (CA) given measurements. However, this Bayesian approach is not well suited for safety-critical applications due to the lack of risk prediction capability, and to the problem of bounding the *a posteriori* probability of association (a similar issue is encountered in [35]). Another insightful approach is followed in [36]. However, it makes approximations that do not necessarily upper-bound risks, hence, do not guarantee safe operation, and it presents exact solutions that could only be evaluated using computationally expensive numerical methods, not adequate for real-time navigation. Also, the risk of FE is not addressed. Overall, research on navigation integrity using FE and DA is sparse.

In response, in this paper, a new, computationally efficient integrity risk prediction method is developed to ensure safety of localization using laser-based FE and DA.

The paper does not present a landmark selection method, but is a key step toward extracting the set of features that maximizes safety performance [37], [38]. The paper assumes either a preestablished map, or prior observations of static landmark features. Many sophisticated algorithms have been devised to extract such features [1]–[15]. For clarity of exposition, the description of the method assumes that each landmark is associated with exactly one extracted feature, and that the number of landmarks in view is constant. Specifics on the FE implementation used in simulation and testing, for extracting point-features and for handling landmarks coming in and out of view, can be found in [39]. In practice, misleading-feature detection and exclusion methods must be used to deal with miss-extracted, nonstatic, and non repeatedly identified features that are not addressed in this paper [38]. Thus, this paper makes assumptions that are not always valid in realistic, unstructured HAV environments, but allow preliminary testing under specific conditions. The starting point of the paper

Authorized licensed use limited to: to IEEExplore provided by University Libraries | Virginia Tech. Downloaded on August 17,2020 at 19:20:58 UTC from IEEE Xplore. Restrictions apply.

is that a matching set of the few most reliably recognizable features are extracted from both current and previous data (or map), with a feature estimation error that can be stochastically bounded using [40], [41].

In Section II of this paper, we develop a multiple-hypothesis innovation-based DA method, which provides the means to predict the probability of IAs considering all potential landmark permutations [42]. In Section III, we derive a probabilistic lower bound on the minimum feature separation, which is guaranteed, at FE, with predefined integrity risk allocation. As compared to our previous conference paper in [42], this new derivation is simpler, and the resulting separation bound is no longer a function of an empirically defined design parameter. In addition, a graphical representation is introduced, which illustrates this probabilistic bound in a normalized separation space. The separation bound is then incorporated in the integrity risk equation. This new method is analyzed and tested in Sections IV and V to quantify the impact of IAs on integrity risk (results are updated as compared to [42]). The following key safety-tradeoff is illustrated: the more measurements are extracted, the lower the integrity risk contribution is under the CA hypothesis, but the higher the other integrity risk contributions become because the risk of IAs increases in the presence of cluttered, poorly distinguishable landmarks. Also, being surrounded by many landmarks increases the probability of continuous, uninterrupted navigation. Concluding notes are given in Section VI.

II. INTEGRITY RISK EVALUATION FOR NAVIGATION USING DATA ASSOCIATION

This section presents a new multiple-hypothesis integrity risk evaluation method for navigation using DA. The integrity risk is first defined in Section II-A: this provides an outline for the remainder of the section, where partial integrity risk contributions are individually evaluated. The "fault-free" component of the integrity risk is derived in Section II-B, assuming CAs. The DA "fault" model is developed in Section II-C, and is used Section II-D to establish an analytical upper bound on the integrity risk accounting for all possible IAs. For readers interested in directly implementing the integrity risk evaluation method, a summary is provided later, in Section III-D.

A. Overall Integrity Risk Equation

Considering the mutually exclusive, exhaustive hypotheses of CA and IA, the probability of hazardous misleading information (HMI) or integrity risk $P(HMI_k)$ at time epoch "k" can be expressed using the law of total probability as follows:

$$\begin{aligned} P(HMI_k) &= P(HMI_k, CA_K) + P(HMI_k, IA_K) \\ &= P(HMI_k|CA_K)P(CA_K) \\ &\quad + P(HMI_k|IA_K)[1 - P(CA_K)] \\ &\leq 1 - [1 - P(HMI_k|CA_K)]P(CA_K) \end{aligned} \quad (1)$$

where

CA_K is the correct association hypothesis for all landmarks at all times.

IA_K is the event regrouping IA hypotheses for any landmark at any past or current time.

We use the notation "capital letter K" to designate a range of indices: $K \equiv \{0, ..., k\}$. In (1), $P(HMI_k|IA_K)$ is safely upper-bounded by $P(HMI_k|IA_K) = 1$. This is a tight bound when the number of extracted landmarks is low because the probability of an IA causing HMI is high.

The DA process is carried out over multiple epochs, all of which are included in the CA_K-event. Let us consider at each time j, for $j = 0, ..., k$, the probability of CA assuming that past associations are all correct: $P(CA_j|CA_{J-1})$. When using SLAM, we define $P(CA_0) \equiv 1$ because there is no association with previous observations at time zero. $P(CA_K)$ can then be iteratively evaluated, without having to make an assumption on the independence of events CA_j, as follows:

$$P(CA_K) = P(CA_0, CA_1, ..., CA_k) = \prod_{j=1}^{k} P(CA_j|CA_{J-1}). \quad (2)$$

Ultimately, the safety criterion is that $P(HMI_k)$ must meet a predefined integrity risk requirement $I_{\mathrm{REQ},k}$, which is set by a certification authority (similar to requirements set for aviation applications in [23]). The integrity risk requirement may be expressed as follows:

$$P(HMI_k) \leq I_{\mathrm{REQ},k}. \quad (3)$$

The next sections provide a method to evaluate $P(HMI_k)$ in (1): $P(HMI_k|CA_K)$ is obtained in Section II-B using the estimation error covariance matrix, and we derive an analytical expression for $P(CA_K)$, or $P(CA_j|CA_{J-1})$, for $j = 0, ..., k$, in (2), in Sections II-C and II-D.

B. Integrity Risk Under Correct Association

1) *Measurement Model and Fault-Free Estimation:* Let n_L be the total number of visible landmarks, and m_F the number of estimated feature parameters per landmark. Feature parameters can include landmark position, orientation, surface properties, etc. (in theory, they can include any property whose measurement error distribution can be modeled using [40], [41]). The total number of feature parameters within the visible landmark set is: $n \equiv n_L m_F$. We can stack the actual (true) values of the extracted feature parameters for all landmarks in an $n \times 1$ vector $\mathbf{z}_k$. Let $\hat{\mathbf{z}}_k$ be an estimate of $\mathbf{z}_k$. We assume that the cumulative distribution function of $\hat{\mathbf{z}}_k$ can be bounded by a Gaussian function with mean $\mathbf{z}_k$ and covariance matrix $\mathbf{V}_k$ [40], [41]. (For example, $\hat{\mathbf{z}}_k$ may comprise laser ranging and bearing measurements—-or linear combinations thereof—-whose distributions are assumed mutually independent and individually bounded.) We use the notation: $\hat{\mathbf{z}}_k \sim N(\mathbf{z}_k, \mathbf{V}_k)$.

For the CA (indicated by the subscript 0) where the ordering of state coefficients matches that of the measurements, the nonlinear measurement equation can be written

Authorized licensed use limited to: to IEEExplore provided by University Libraries | Virginia Tech. Downloaded on August 17,2020 at 19:20:58 UTC from IEEE Xplore. Restrictions apply.

in terms of the system state parameter vector $\mathbf{x}_k$ as follows:

$$\hat{\mathbf{z}}_k = \mathbf{h}_{0,k}(\mathbf{x}_k) + \mathbf{v}_k \tag{4}$$

where

$\mathbf{x}_k$ is the state vector, which includes vehicle pose parameters, and may also include constant landmark feature parameters when using a SLAM-type approach [2], [8], [27], as will be the case in Sections IV and V. Let m be the number of state parameters to be estimated. $\mathbf{x}_k$ is an $m \times 1$ vector.

$\mathbf{v}_k$ is the extracted measurement noise vector: $\mathbf{v}_k \sim N(\mathbf{0}_{n\times 1}, \mathbf{V}_k)$, where $\mathbf{0}_{a\times b}$ is an $a \times b$ matrix of zeros.

It is worth noting that, under the CA hypothesis, the mean of $\hat{\mathbf{z}}_k$ is: $\mathbf{z}_k = \mathbf{h}_{0,k}(\mathbf{x}_k)$. Therefore, we can write

$$\hat{\mathbf{z}}_k \sim N\left(\mathbf{h}_{0,k}(\mathbf{x}_k), \mathbf{V}_k\right). \tag{5}$$

Equation (4) can be linearized about an estimate $\bar{\mathbf{x}}_k$ of $\mathbf{x}_k$

$$\begin{aligned}\hat{\mathbf{z}}_k &= \mathbf{h}_{0,k}(\mathbf{x}_k) + \mathbf{h}_{0,k}(\bar{\mathbf{x}}_k) - \mathbf{h}_{0,k}(\bar{\mathbf{x}}_k) + \mathbf{v}_k \\ &\approx \mathbf{h}_{0,k}(\bar{\mathbf{x}}_k) + \mathbf{H}_k(\mathbf{x}_k - \bar{\mathbf{x}}_k) + \mathbf{v}_k \end{aligned} \tag{6}$$

where $\mathbf{H}_k \equiv \frac{\partial \mathbf{h}_{0,k}(\mathbf{x}_k)}{\partial \mathbf{x}_k}|_{\bar{\mathbf{x}}_k}$,

$$\mathbf{H}_k(\mathbf{x}_k - \bar{\mathbf{x}}_k) \approx \mathbf{h}_{0,k}(\mathbf{x}_k) - \mathbf{h}_{0,k}(\bar{\mathbf{x}}_k). \tag{7}$$

Subscript 0 is not added to $\mathbf{H}_k$, which always assumes CA.

In addition, a linear model is assumed for the propagation of state parameters over time

$$\mathbf{x}_k = \Phi_{k-1}\mathbf{x}_{k-1} + \mathbf{w}_{k-1}. \tag{8}$$

The following assumption is made for the process noise $\mathbf{w}_{k-1}$: $\mathbf{w}_{k-1} \sim N(\mathbf{0}, \mathbf{W}_{k-1})$.

For the system model described in (4) and (8), an EKF is used to estimate $\mathbf{x}_k$. The state prediction vector, prediction error covariance matrix, state estimate vector, and state estimate error covariance matrix are, respectively, given by the following:

$$\bar{\mathbf{x}}_k = \Phi_{k-1}\hat{\mathbf{x}}_{k-1}, \quad \bar{\mathbf{P}}_k = \Phi_{k-1}\hat{\mathbf{P}}_{k-1}\Phi_{k-1}^T + \mathbf{W}_{k-1} \tag{9}$$

$$\hat{\mathbf{x}}_k = \bar{\mathbf{x}}_k + \mathbf{K}_k\gamma_{0,k}, \quad \hat{\mathbf{P}}_k = (\mathbf{I} - \mathbf{K}_k\mathbf{H}_k)\bar{\mathbf{P}}_k \tag{10}$$

where $\mathbf{K}_k$ is the Kalman gain, $\mathbf{K}_k = \bar{\mathbf{P}}_k\mathbf{H}_k^T(\mathbf{H}_k\bar{\mathbf{P}}_k\mathbf{H}_k^T + \mathbf{V}_k)^{-1}$, and $\gamma_{0,k}$ is the $n \times 1$ innovation vector, under the CA hypothesis (subscript 0)

$$\gamma_{0,k} \equiv \hat{\mathbf{z}}_k - \mathbf{h}_{0,k}(\bar{\mathbf{x}}_k). \tag{11}$$

The estimation error is defined as follows:

$$\hat{\varepsilon}_k \equiv \hat{\mathbf{x}}_k - \mathbf{x}_k. \tag{12}$$

Let us define the hazard state as the element, or linear combination of elements in $\mathbf{x}_k$, that is, of primary concern for navigation safety. For example, for steering a vehicle to remain within a lane on a highway, the focus is placed on the positioning error in the direction perpendicular to the lane. The estimation error $\hat{\varepsilon}_k$ for the state of interest is given by the following:

$$\hat{\varepsilon}_k \equiv \alpha^T\hat{\varepsilon}_k \tag{13}$$

where α is a vector of predefined coefficients, for example, all zeros and a one for the East position coordinate when travelling on a North–South road. Let σ_k^2 be the estimation error variance for the state of interest, under the CA hypothesis: $\hat{\varepsilon}_k \sim N(0, \sigma_k^2)$. The challenge in this paper is to evaluate the impact on $\hat{\varepsilon}_k$ of errors in FE and DA.

2) *Integrity Risk Under Correct Association:* Under the CA hypothesis, the integrity risk can be directly derived from σ_k^2. The integrity risk is defined as the probability of the estimation error $\hat{\varepsilon}_k$ exceeding a predefined limit of acceptability, also called alert limit ℓ (as specified, for example, in [23] for aviation applications)

$$P(HMI_k) \equiv P\left(|\hat{\varepsilon}_k| > \ell\right). \tag{14}$$

We have seen that under the CA hypothesis, the distribution of $\hat{\varepsilon}_k$ is known: $\hat{\varepsilon}_k \sim N(0, \sigma_k^2)$. Therefore, $P(HMI_k|CA_K)$ is given by the following:

$$\begin{aligned}P(HMI_k|CA_K) &= P\left(|\hat{\varepsilon}_k| < \ell \mid CA_K\right) \\ &\le Q\left(\frac{\ell}{\sigma_k}\right) + 1 - Q\left(\frac{-\ell}{\sigma_k}\right)\end{aligned} \tag{15}$$

where $Q()$ is the tail probability function of the standard normal distribution.

The variance σ_k^2 is often used to evaluate laser-based navigation system performance (e.g., in [8]). Equation (1) shows that σ_k^2 is an insufficient metric in safety-critical applications because $P(CA_K)$ must be accounted for. Evaluating $P(CA_K)$ is challenging, and is the focus of the rest of this section.

C. The Incorrect Association Problem and the Relevance of the Innovation Vector

The IA differs from other fault modes in sensor-based navigation (such as, for example, GPS satellite clock faults causing ranging errors of all magnitudes) in that there is only a finite number of ways the DA process can fail. We can exploit this characteristic in a multiple hypothesis approach.

At the FE step, all feature measurements $\hat{\mathbf{z}}_k$ at time-index "k" are known for an arbitrary ordering of the landmarks. If n_L landmarks are extracted at time k, there are $(n_L!)$ potential landmark permutations, i.e., $(n_L!)$ ways to arrange the measurement (4), which we call $(n_L!)$ candidate associations. (Following the assumptions made in Section I, the total number of mapped landmarks—-or of previously observed landmarks when using SLAM—- is also the number n_L of extracted landmarks.) Landmark selection [37], [38] can be implemented to limit n_L.

IA occurs when the ordering of measurements in $\hat{\mathbf{z}}_k$ does not match the assumed ordering of landmarks in $\bar{\mathbf{z}}_{i,k}$, which in SLAM is simply: $\bar{\mathbf{z}}_{i,k} = \mathbf{h}_{i,k}(\bar{\mathbf{x}}_k)$. Subscript i designates association hypotheses, for $i = 0, ..., h$, where $h = n_L! - 1$. We define $i = 0$ the fault-free, CA hypothesis, the other h hypotheses are IA.

DA impacts the EKF estimation process in (10) through the innovation vector $\gamma_{i,k}$ defined in (11) for the CA-case. $\gamma_{i,k}$ is an effective indicator of CA because it is zero mean

Authorized licensed use limited to: to IEEExplore provided by University Libraries | Virginia Tech. Downloaded on August 17,2020 at 19:20:58 UTC from IEEE Xplore. Restrictions apply.

only if the CA was selected (recall that the mean of $\hat{\mathbf{z}}_k$ in (5) is $\mathbf{h}_{0,k}(\mathbf{x}_k)$).

In all IA cases, the mean of $\gamma_{i,k}$ is not zero, and is expressed in terms of $n \times n$ permutation matrices $\mathbf{A}_{i,k}$, for $i = 1, ..., h$, as follows:

$$\begin{aligned}\gamma_{i,k} &= \hat{\mathbf{z}}_k - \mathbf{h}_{i,k}(\bar{\mathbf{x}}_k) \\ &= \mathbf{h}_{0,k}(\mathbf{x}_k) + \mathbf{v}_k - \mathbf{h}_{i,k}(\bar{\mathbf{x}}_k) + \mathbf{h}_{i,k}(\mathbf{x}_k) - \mathbf{h}_{i,k}(\mathbf{x}_k) \\ &\approx \mathbf{y}_{i,k} + \mathbf{v}_k - \mathbf{A}_{i,k}\mathbf{H}_k\bar{\varepsilon}_k \end{aligned} \tag{16}$$

where

$$\mathbf{h}_{i,k} \equiv \mathbf{A}_{i,k}\mathbf{h}_{0,k} \tag{17}$$

$$\mathbf{y}_{i,k} \equiv \mathbf{B}_{i,k}\mathbf{h}_{0,k}(\mathbf{x}_k), \quad \mathbf{y}_{0,k} = \mathbf{0} \tag{18}$$

$$\mathbf{B}_{i,k} \equiv \mathbf{I}_n - \mathbf{A}_{i,k}$$

$$\bar{\varepsilon}_k \equiv \bar{\mathbf{x}}_k - \mathbf{x}_k \tag{19}$$

and where $\mathbf{I}_a$ is the $a \times a$ identity matrix.

As an illustrative example, consider the case where IA hypothesis "$i = 1$" designates the event where landmark "1" is mistaken for landmark "2." $\mathbf{A}_{i,k}$ and $\mathbf{B}_{i,k}$ take the following forms (where m_F is the number of feature parameters per landmark):

$$\mathbf{A}_1 = \begin{bmatrix} \mathbf{0}_{m_F \times m_F} & \mathbf{I}_{m_F} & \mathbf{0}_{m_F \times (n-2m_F)} \\ \mathbf{I}_{m_F} & \mathbf{0}_{m_F \times m_F} & \mathbf{0}_{m_F \times (n-2m_F)} \\ \mathbf{0}_{(n-2m_F) \times m_F} & \mathbf{0}_{(n-2m_F) \times m_F} & \mathbf{I}_{n-2m_F} \end{bmatrix}$$

$$\mathbf{B}_{1,k} = \begin{bmatrix} \mathbf{I}_{m_F} & -\mathbf{I}_{m_F} & \mathbf{0}_{m_F \times (n-2m_F)} \\ -\mathbf{I}_{m_F} & \mathbf{I}_{m_F} & \mathbf{0}_{m_F \times (n-2m_F)} \\ \mathbf{0}_{(n-2m_F) \times m_F} & \mathbf{0}_{(n-2m_F) \times m_F} & \mathbf{0}_{(n-2m_F) \times (n-2m_F)} \end{bmatrix}$$

Equation (16) shows that an IA simultaneously affects multiple measurements, and that it causes a shift $\mathbf{y}_{i,k}$ in the mean of $\gamma_{i,k}$ as compared to $\gamma_{0,k}$, as well as a modification of the random errors from $\mathbf{H}_k\bar{\varepsilon}_k$ for CA to $\mathbf{A}_i\mathbf{H}_k\bar{\varepsilon}_k$ for IA.

D. Data Association Criterion

To lighten notations in Sections II-D and in Sections III-A–III-C, we drop the time subscript k. We also drop the conditional '$|CA_{K-1}$' in (1) and (2), with the understanding that probabilities of correct and IAs at time k, $P(CA)$ and $P(IA)$, assume that all prior associations are correct.

1) *Data Association Criterion:* The nearest neighbor association criterion [1] is defined by the minimum norm of innovation vector γ_i, weighted by the inverse innovation covariance matrix $\mathbf{Y}_i^{-1}$, over all possible landmark permutations $i = 0, ..., h$. The association criterion is expressed as follows:

$$\min_{i=0,...,h} \|\gamma_i\|_{\mathbf{Y}_i^{-1}} \tag{20}$$

$$\text{where } \|\gamma_i\|_{\mathbf{Y}_i^{-1}} = \sqrt{\gamma_i^T \mathbf{Y}_i^{-1} \gamma_i}, \quad \mathbf{Y}_i = \mathbf{A}_i\mathbf{H}\bar{\mathbf{P}}\mathbf{H}^T\mathbf{A}_i^T + \mathbf{V}. \tag{21}$$

The weighted norm operator $\|\,\|_\Omega$ with weighting matrix Ω is used throughout the remainder of the paper.

2) *Example Innovation Space Representation:* To illustrate the criterion in (20), we use the one-dimensional (1D) example displayed in Fig. 2.

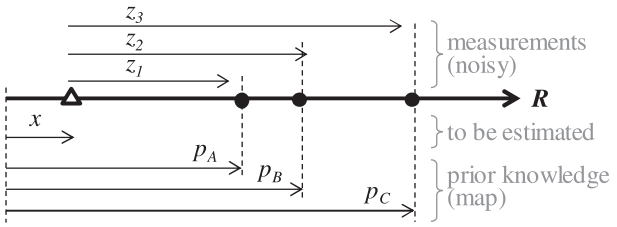

Fig. 2. Illustrative one-dimensional example of a sensor (at location x in reference $\boldsymbol{R}$) providing observations to three landmarks. The sensor is at location x in reference frame $\boldsymbol{R}$, and the three landmarks are at locations p_A, p_B, and p_C. Sensor to landmark measurements are noted z_1, z_2, and z_3.

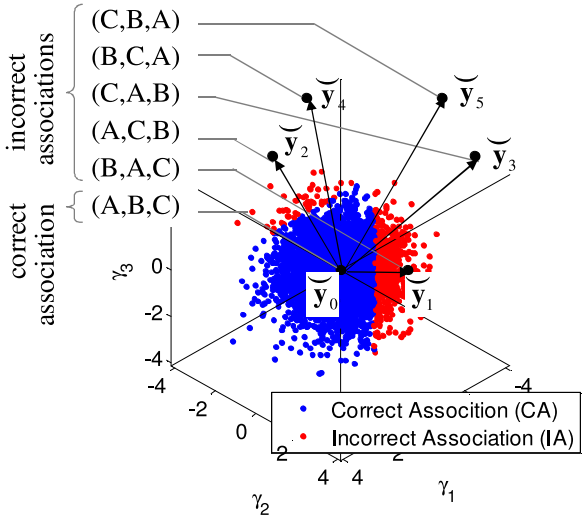

Fig. 3. Innovation-space representation of the assoication process. The ratio of blue samples over the total number of samples is the probability of correct association.

The problem in Fig. 2 is to estimate the position x of the sensor (upward pointing triangle) on a 1D navigation reference axis $\boldsymbol{R}$, given the positions p_A, p_B, and p_C of three landmarks on $\boldsymbol{R}$ (black circles), and using a set of noisy relative measurements z_1, z_2, and z_3 between sensor and landmarks. The challenge of DA is, in the presence of sensor errors, to find the ordering of landmarks $\{p_A, p_B, p_C\}$ corresponding the ordering of measurements $\{z_1, z_2, z_3\}$.

In this instance, the number of landmarks is $n_L = 3$, and the number of possible permutations is $(n_L!) = 6$, i.e., we consider six innovation vectors γ_i. Vector γ_i is zero-mean only for the CA $i = 0$, which is why the association criterion in (20) selects the minimum norm $\|\gamma_i\|_{\mathbf{Y}_i^{-1}}$.

The DA criterion is represented in innovation space in Fig. 3. In this example, the number of features per landmark is $m_F = 1$, and the innovation space is 3D ($n = n_L m_F = 3$). The impact of DA on the mean normalized innovation vectors $\breve{\mathbf{y}}_i \equiv \mathbf{Y}_i^{-1/2}\mathbf{y}_i$ can be represented for all six landmark permutations, for $i = 0, ..., 5$. Vectors $\breve{\mathbf{y}}_i$ lay in a space of dimension $n - m_F$, in this case, in a plane, and $\breve{\mathbf{y}}_0$ is at the origin.

In addition, in Fig. 3, 10 000 random samples of measurements z_1, z_2, and z_3 were simulated. Equation (20) was

Authorized licensed use limited to: to IEEExplore provided by University Libraries | Virginia Tech. Downloaded on August 17,2020 at 19:20:58 UTC from IEEE Xplore. Restrictions apply.

used to distinguish correctly associated samples in blue, from incorrectly associated samples in red. The probability of CA $P(CA)$, which we are trying to determine, is ratio of blue samples over the total number of samples. The next paragraphs provide an analytical expression for $P(CA)$.

3) *Probability of Correct Association:* IA occurs if, for any i other than 0, the following inequality is verified:

$$\|\gamma_i\|_{\mathbf{Y}_i^{-1}} \leq \|\gamma_0\|_{\mathbf{Y}_0^{-1}}. \tag{22}$$

Anticipating the fact that the correlation between γ_i and γ_0 has to be accounted for, (16) is rewritten as follows:

$$\gamma_i = \mathbf{y}_i + \left[\mathbf{I} \; -\mathbf{A}_i\mathbf{H}\right]\begin{bmatrix}\mathbf{v}\\ \bar{\varepsilon}\end{bmatrix} = \mathbf{y}_i + \mathbf{M}_i^T\mathbf{r} \tag{23}$$

where

$$\mathbf{M}_i \equiv \begin{bmatrix}\mathbf{I}\\ -\mathbf{A}_i\mathbf{H}\end{bmatrix}, \quad \mathbf{r} \equiv \begin{bmatrix}\mathbf{v}\\ \bar{\varepsilon}\end{bmatrix} \tag{24}$$

$$\mathbf{r} \sim N\left(\mathbf{0}, \mathbf{R} \equiv \begin{bmatrix}\mathbf{V} & \mathbf{0}\\ \mathbf{0} & \bar{\mathbf{P}}\end{bmatrix}\right). \tag{25}$$

Substituting (23) into (22), we can write the following inequality:

$$\|\mathbf{y}_i\|_{\mathbf{Y}_i^{-1}} - \left\|\mathbf{M}_i^T\mathbf{r}\right\|_{\mathbf{Y}_i^{-1}} \leq \left\|\mathbf{M}_0^T\mathbf{r}\right\|_{\mathbf{Y}_0^{-1}} \tag{26}$$

because it is always true that

$$\|\mathbf{y}_i\|_{\mathbf{Y}_i^{-1}} - \left\|\mathbf{M}_i^T\mathbf{r}\right\|_{\mathbf{Y}_i^{-1}} \leq \left\|\mathbf{y}_i + \mathbf{M}_i^T\mathbf{r}\right\|_{\mathbf{Y}_i^{-1}}. \tag{27}$$

Equation (26) is equivalent to

$$\|\mathbf{y}_i\|_{\mathbf{Y}_i^{-1}} \leq \left\|\mathbf{M}_0^T\mathbf{r}\right\|_{\mathbf{Y}_0^{-1}} + \left\|\mathbf{M}_i^T\mathbf{r}\right\|_{\mathbf{Y}_i^{-1}}. \tag{28}$$

Let us define the $(n+m)\times 1$ vector of independently, identically distributed random variables $\mathbf{q} \equiv \mathbf{R}^{-1/2}\mathbf{r}$. We have: $\mathbf{q} \sim N(\mathbf{0}_{(n+m)\times 1}, \mathbf{I}_{n+m})$. Also, let $\lambda^2_{\mathrm{MAX},i}$ and $\lambda^2_{\mathrm{MAX},0}$, respectively, be the maximum eigenvalues of $\mathbf{R}^{1/2}(\mathbf{M}_i\mathbf{Y}_i^{-1}\mathbf{M}_i^T)\mathbf{R}^{1/2}$ and $\mathbf{R}^{1/2}(\mathbf{M}_0\mathbf{Y}_0^{-1}\mathbf{M}_0^T)\mathbf{R}^{1/2}$. We use an upper-bound for the right-hand side of (28)

$$\|\mathbf{y}_i\|_{\mathbf{Y}_i^{-1}} \leq \sqrt{\mathbf{q}^T\mathbf{q}}\left(\lambda_{\mathrm{MAX},i} + \lambda_{\mathrm{MAX},0}\right). \tag{29}$$

The appendix shows that $\lambda^2_{\mathrm{MAX},i} = 1$ and $\lambda^2_{\mathrm{MAX},0} = 1$, so that (29) is equivalent to

$$q^2 \geq \frac{y_i^2}{4} \tag{30}$$

where

$$q^2 \equiv \mathbf{q}^T\mathbf{q} \;\;, \quad y_i^2 \equiv \|\mathbf{y}_i\|^2_{\mathbf{Y}_i^{-1}} \tag{31}$$

where q^2 is chi-squared distributed with $n+m$ degrees of freedom (DOF) (where $n+m$ is the number of measurements n plus the number of states m, i.e., the length of $\mathbf{v}$ plus length of $\bar{\varepsilon}$).

It follows that the probability of CA $P(CA)$ can be lower-bounded using the following inequality:

$$\begin{aligned} P(CA) &= 1 - P(IA)\\ &= 1 - P\left(\bigcup_{i=1}^{h}\|\gamma_i\|^2_{\mathbf{Y}_i^{-1}} \leq \|\gamma_0\|^2_{\mathbf{Y}_0^{-1}}\right)\\ &\geq 1 - P\left(\bigcup_{i=1}^{h} q^2 \geq \frac{y_i^2}{4}\right)\\ &\geq 1 - P\left(q^2 \geq \min_{i=1,\ldots,h}\left(\frac{y_i^2}{4}\right)\right). \end{aligned} \tag{32}$$

Substituting (32) into (2) for $P(CA_j|CA_{J-1})$, and the result into (1), provides an upper-bound on the integrity risk $P(HMI_k)$.

Equation (32) is expressed in terms of the norm squared y_i^2 of the mean normalized innovation vectors $\breve{\mathbf{y}}_i$ represented in Fig. 3. However, in practice, we do not know $\breve{\mathbf{y}}_i$; all we are given is one sample of γ_i. Fortunately, FE provides a means to establish a lower bound on y_i^2.

III. EXTRACTED FEATURE SEPARATION MEASURE

Our approach to bound $P(HMI_k)$ leverages the FE step to ensure that landmark features (position, orientation, reflectivity, . . . ,) are distinguishable, hence, easier to associate. The objective is to guarantee, with quantifiable integrity, that there is a minimum separation between landmark features.

The minimum separation can be computed at FE without requiring DA. Within a set of features, this minimum separation is determined by considering all possible permutations. This multiple-hypothesis approach purposely mirrors that used in Section II, and is adopted to exploit the relationship between mean separation vectors and mean EKF innovation vectors.

Section III-A first describes a normalized measure of separation between landmark features. A probabilistic lower-bound on this separation is given in Section III-B, and mapped to innovation space in Section III-C to assess the impact of feature separation on integrity. Section III-D summarizes the entire integrity risk evaluation method, as described in Sections II and III.

A. Feature Separation Measure

The minimum feature separation is evaluated using mapped (or previously observed) features $\bar{\mathbf{z}}$. Under Section I's assumption that extracted landmarks match mapped landmarks, we will show that this minimum separation provides a lower-bound on mean innovation vectors (in Section III-C). Cases where Section I's assumption is not satisfied will be addressed in future work by FE algorithm design and by misleading-feature detection/exclusion.

To lighten notations, in Sections III-A–III-C, we have dropped subscripts for time (k) and for the ordering-with-respect-to-$\hat{\mathbf{z}}$ (i), which are not relevant at the FE step, so that $\bar{\mathbf{z}} = \bar{\mathbf{z}}_{i,k}$. Vector $\bar{\mathbf{z}}$ is an $n\times 1$ vector obtained by stacking all previously observed feature parameters: $\bar{\mathbf{z}} \sim N(\mathbf{z}, \bar{\mathbf{V}})$.

Authorized licensed use limited to: to IEEExplore provided by University Libraries | Virginia Tech. Downloaded on August 17,2020 at 19:20:58 UTC from IEEE Xplore. Restrictions apply.

We consider a comprehensive set of nonidentity landmark permutation matrices, so that matrices $\mathbf{B}_l \equiv \mathbf{I}_n - \mathbf{A}_{l,k}$, for $l = 1, ..., h$, can be computed. The set of $\mathbf{A}_l$ matrices is the same as the set of $\mathbf{A}_{i,k}$ in (16), but we are excluding the identity permutation noted $\mathbf{A}_0$ for $l = 0$. For a permutation l, the landmark "separation" vector is defined as follows:

$$\bar{\mathbf{d}}_l \equiv \mathbf{B}_l \bar{\mathbf{z}} \quad \text{and} \quad \bar{\mathbf{d}}_l \sim N(\mathbf{y}_l, \mathbf{D}_l) \tag{33}$$

where

$$\mathbf{y}_l = \mathbf{B}_l \mathbf{z} \text{ in (18), and } \mathbf{D}_l \equiv \mathbf{B}_l \bar{\mathbf{V}} \mathbf{B}_l^T. \tag{34}$$

It is worth noting that $\mathbf{B}_l$ is rank deficient, with rank values ranging from m_F to $n - m_F$ depending on how many landmarks are involved in permutation l, for $l = 1, ..., h$. Let r_l be the rank of $\mathbf{B}_l$. An orthogonal decomposition of the symmetric positive semi definite matrix $\mathbf{D}_l$ is expressed as follows:

$$\mathbf{D}_l = \begin{bmatrix} \mathbf{U}_l & \mathbf{U}_{l,0} \end{bmatrix} \begin{bmatrix} \mathbf{S}_l & \mathbf{0} \\ \mathbf{0} & \mathbf{0} \end{bmatrix} \begin{bmatrix} \mathbf{U}_l^T \\ \mathbf{U}_{l,0}^T \end{bmatrix} = \mathbf{U}_l \mathbf{S}_l \mathbf{U}_l^T \tag{35}$$

where $\mathbf{S}_l$ is a $r_l \times r_l$ diagonal matrix of non-zero singular values, and $\mathbf{U}_l$ is a $n \times r_l$ matrix such that $\mathbf{U}_l^T \mathbf{U}_l = \mathbf{I}_{r_l}$. For each permutation, we can define the $r_l \times 1$ normalized separation vector $\bar{\eta}_l$ as follows:

$$\bar{\eta}_l \equiv \mathbf{S}_l^{-1/2} \mathbf{U}_l^T \bar{\mathbf{d}}_l \tag{36}$$

$$\bar{\eta}_l \sim N(\eta_l, \mathbf{I}_{r_l}), \quad \text{where } \eta_l \equiv \mathbf{S}_l^{-1/2} \mathbf{U}_l^T \mathbf{d}_l. \tag{37}$$

The norm squared $\bar{d}_l^2$ of $\bar{\eta}_l$ is a measure of separation for permutation l, and can be written as follows:

$$\bar{d}_l^2 \equiv \bar{\eta}_l^T \bar{\eta}_l = \bar{\mathbf{d}}_l^T \mathbf{U}_l \mathbf{S}_l^{-1} \mathbf{U}_l^T \bar{\mathbf{d}}_l. \tag{38}$$

Using the norm operator, $\bar{d}_l$ can be expressed as: $\bar{d}_l = \|\bar{\eta}_l\|$ (the weighting matrix is $\mathbf{I}_{r_l}$). $\bar{d}_l^2$ is noncentrally chi-square distributed with r_l DOF and with noncentrality parameter d_l^2 defined as: $d_l^2 \equiv \|\eta_l\|^2$. We use the notation: $\bar{d}_l^2 \sim \chi^2(r_l, d_l^2)$.

Finally, the overall landmark separation metric is the minimum feature separation defined as follows:

$$\bar{d} \equiv \min_{l=1,..,h} (\bar{d}_l). \tag{39}$$

B. Lower-Bound on Feature Separation

1) *Lower Bound Derivation:* This subsection aims at establishing an integrity bound L_D on the true minimum separation between landmarks d, given an estimate $\bar{d}$ obtained from prior information $\bar{\mathbf{z}}$. In mathematical terms, we want to find a L_D to satisfy the following:

$$P(d < L_D | \bar{d}) \leq I_{\text{FE,ALLOC}} \tag{40}$$

where $I_{\text{FE,ALLOC}}$ is a small portion of the overall integrity risk requirement I_{REQ} allocated to the bound L_D at FE ($I_{\text{FE,ALLOC}} << I_{\text{REQ}}$). L_D and d are unknown, but $I_{\text{FE,ALLOC}}$ and $\bar{d}$ are given and $\bar{d}$ provides a noisy measure of d. It is worth noting that $\bar{d}$ is considered "prior knowledge" in the sense that it is not derived from current measurements ($\bar{d}$ can be obtained from a map). The following probabilities are expressed given $\bar{d}$ to remind ourselves that $\bar{d}$ is known while d is not, but these probabilities are not Bayesian, i.e., not based on current measurements.

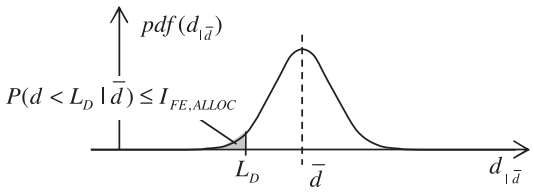

Fig. 4. One-degree-of-freedom representation for the derivation of L_D. Given a sample estimate $\bar{d}$, our knowledge of d is uncertain; this uncertainty is represented with a Gaussian shell.

The risk $P(d < L_D | \bar{d})$ is bounded using the following inequalities:

$$\begin{aligned} P(d < L_D | \bar{d}) &= P(\bar{d} - d > \bar{d} - L_D | \bar{d}) \\ &\leq P\left(\|\bar{\eta}\| - \|\eta\| > \bar{d} - L_D | \bar{d}\right) \\ &\leq P\left(\|\bar{\eta} - \eta\| > \bar{d} - L_D | \bar{d}\right) \\ &\leq P\left(\bar{\varepsilon}_D > \bar{d} - L_D | \bar{d}\right) \end{aligned} \tag{41}$$

where

$$\bar{\varepsilon}_D \equiv \|\bar{\eta} - \eta\| \text{ and } \bar{\eta} \equiv \bar{\eta}_{l_{MIN}} \text{ for } l_{\text{MIN}} \equiv \arg \min_{l=1,..,h} (\bar{d}_l)$$

and where we used the reverse triangle inequality

$$\bar{d} - d = \|\bar{\eta}\| - \|\eta\| \leq |\, \|\bar{\eta}\| - \|\eta\| \,| \leq \|\bar{\eta} - \eta\|.$$

Fig. 4 provides an illustration of the variables in (41) for a hypothetical single- DOF distribution of d-given-$\bar{d}$, noted $d_{|\bar{d}}$, whose probability density function can be represented as a Gaussian function. We determine L_D such that the probability of $d_{|\bar{d}}$ lower than L_D' is equal to $I_{\text{FE,ALLOC}}$.

There can be cases where landmarks are not reliably distinguishable, i.e., where $\bar{d}$ is small so that there is no positive L_D that achieves $P(\bar{\varepsilon}_D > \bar{d} - L_D | \bar{d}) \leq I_{\text{FE,ALLOC}}$. Such cases can be easily and unambiguously identified, and therefore pose no threat to integrity. They may cause loss of navigation availability or continuity (as defined in [23] for aviation applications), which can be mitigated by relaxing the requirement $I_{\text{FE,ALLOC}}$, or by landmark clustering and selection as described in [38]. With regard to integrity, we choose to proceed only if we can find L_D such that $\bar{d} - L_D > 0$. It follows that (41) can be further bounded by

$$P(d < L_D | \bar{d}) \leq P\left(\bar{\varepsilon}_D^2 > (\bar{d} - L_D)^2 | \bar{d}\right). \tag{42}$$

The separation error $\bar{\varepsilon}_D^2$ is centrally chi-square distributed with a number of DOF r: $m_F \leq r \leq n - m_F$. It is conservative with respect to integrity risk to assume $\bar{\varepsilon}_D^2 \sim \chi^2(m_F, 0)$. Thus, the lower bound L_D is determined using the equation

$$\begin{aligned} P\left(\bar{\varepsilon}_D^2 > (\bar{d} - L_D)^2 | \bar{d}\right) &= \int_{(\bar{d} - L_D)^2}^{+\infty} \chi_\alpha^2(m_F, 0) d\alpha \\ &= I_{\text{FE,ALLOC}}. \end{aligned} \tag{43}$$

L_D can also be expressed as: $L_D = \bar{d} - \sqrt{\chi_{m_F}^{-2}(1 - I_{\text{FE,ALLOC}})}$, where $\chi_{m_F}^{-2}()$ is the inverse chi-square distribution with m_F DOF. $\bar{d}$ being too small can yield negative L_D-values, which we exclude. $\bar{d}$ being too large as compared to d can yield

Authorized licensed use limited to: to IEEExplore provided by University Libraries | Virginia Tech. Downloaded on August 17,2020 at 19:20:58 UTC from IEEE Xplore. Restrictions apply.

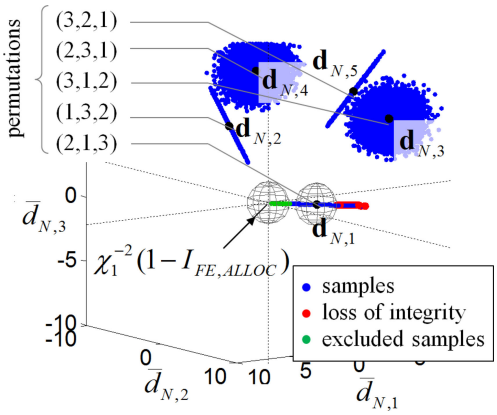

Fig. 5. Separation-space representation of separation vectors for the illustrative one-dimensional example described in Fig. 2.

misleadingly large L_D-values, which can cause loss of integrity, but will occur with probability lower than $I_{\text{FE,ALLOC}}$.

2) *Example Separation-Space Representation:* The 1D three-landmark example shown in Fig. 2 is used here again to illustrate the separation bound derived in (33)–(43). Because the normalized separation vectors $\bar{\eta}_l$ are of different dimensions, we introduce a normalized separation vector $\bar{\mathbf{d}}_{N,l}$ defined as: $\bar{\mathbf{d}}_{N,l} \equiv \mathbf{U}_l^T \bar{\eta}_l$.

Fig. 5 shows the mean normalized vectors $\mathbf{d}_{N,l}$, for $l = 1, ..., 5$, in 3D separation space (represented with black dots). Their spatial distribution is similar to that of the mean innovation vectors in Fig. 3. We will rigorously explore this relationship in Section III-C. In addition, Fig. 5 presents 10 000 samples of $\bar{\mathbf{d}}_{N,l}$, for $l = 1, ..., 5$. As expected from the dimensions of $\bar{\eta}_l$, sample separation vectors for permutations involving two landmarks (labeled "1," "2," and "5") lay along lines, whereas separation vectors for the two triple-landmark permutations ("3" and "4") lay on a plane.

Fig. 5 also shows color-coded sample data points, and two spheres of radius $\sqrt{\chi_{m_F}^{-2}(1-I_{\text{FE,ALLOC}})}$ centered at the origin and at the smallest mean separation vector $\mathbf{d}_{N,1}$. As explained above, cases where the norm of $\bar{\mathbf{d}}_{N,l}$ is too small can cause L_D to be negative, and can simply be excluded. These data points are shown in green. In parallel, cases where the norm of $\bar{\mathbf{d}}_{N,l}$ is significantly larger than that of $\mathbf{d}_{N,l}$ can cause misleadingly large separation bound L_D. These data points shown in red can cause loss of integrity, but occur with a probability lower than $I_{\text{FE,ALLOC}}$.

C. Incorporating the Separation Bound Into the Integrity Risk Equation

First, we use the law of total probability to express the integrity risk as (we drop the condition "$|\bar{d}$" to lighten notations)

$$\begin{aligned} P(HMI_k) &\le P(HMI_k, d < L_D) + P(HMI_k, d \ge L_D) \\ &\le P(d < L_D) + P(HMI_k | d \ge L_D) P(d \ge L_D) \\ &\le I_{\text{FE,ALLOC},k} + P(HMI_k | d \ge L_D) \end{aligned}$$

where we used (40). We can determine $P(HMI_k|d \ge L_D)$ using (1) with the knowledge that the unknown d is larger than L_D. Therefore, we can find $P(CA)$ in (32) given that $d \ge L_D$ (to lighten notations, we do not explicitly include condition "$|d \ge L_D$").

Then, (33)–(43) can be used to address the fact that y_i^2 in (32) is unknown. y_i^2, which is defined in (31), is rewritten by pre and postmultiplying the weighting matrix $\mathbf{Y}_i^{-1}$ by the identity matrix $(\mathbf{U}_i\mathbf{S}_i^{-1/2}\mathbf{U}_i^T)(\mathbf{U}_i\mathbf{S}_i^{1/2}\mathbf{U}_i^T)$

$$y_i^2 = \mathbf{y}_i^T \mathbf{U}_i \mathbf{S}_i^{-1/2} \mathbf{U}_i^T (\mathbf{U}_i \mathbf{S}_i^{1/2} \mathbf{U}_i^T \mathbf{Y}_i^{-1} \mathbf{U}_i \mathbf{S}_i^{1/2} \mathbf{U}_i^T) \mathbf{U}_i \mathbf{S}_i^{-1/2} \mathbf{U}_i^T \mathbf{y}_i \tag{44}$$

y_i^2 can be lower-bounded using the following inequality:

$$y_i^2 \ge \mathbf{y}_i^T \mathbf{U}_i \mathbf{S}_i^{-1} \mathbf{U}_i^T \mathbf{y}_i \lambda_{MIN,i}^2 \tag{45}$$

where $\lambda_{\text{MIN},i}^2$ is the minimum eigenvalue of $(\mathbf{U}_i\mathbf{S}_i^{1/2}\mathbf{U}_i^T\mathbf{Y}_i^{-1}\mathbf{U}_i\mathbf{S}_i^{1/2}\mathbf{U}_i^T)$.

In addition, without loss of generality since we consider all nonidentity permutations, and to avoid introducing a new notation, let us assume that the ordering of landmark features in $\bar{\mathbf{z}}$ in (33) and $\hat{\mathbf{z}}$ in (4) is the same, so that their mean vector $\mathbf{z}$ is identical. The mean innovation vector under IA hypotheses in (16) and the mean separation vector in (33) are identical, but with different indices

$$\mathbf{y}_i \equiv \mathbf{B}_i \mathbf{z} \text{ for } i = 1, ..., h \text{ and } \mathbf{y}_l \equiv \mathbf{B}_l \mathbf{z} \text{ for } l = 1, ..., h.$$

Thus, (43) establishes with probability larger or equal to $1 - I_{\text{FE,ALLOC}}$ that the following bound holds:

$$d_i^2 = \mathbf{y}_i^T \mathbf{U}_i \mathbf{S}_i^{-1} \mathbf{U}_i^T \mathbf{y}_i \ge d^2 \ge L_D^2. \tag{46}$$

Substituting, (46) into (45), y_i^2 can be further lower-bounded by

$$y_i^2 \ge L_D^2 \lambda_{\text{MIN},i}^2. \tag{47}$$

Equation (47) is used to establish an analytical bound on $P(CA)$ in (32), which is now expressed in terms of all known quantities as follows:

$$P(CA) \ge 1 - P\left(q^2 \ge \min_{i=1,...,h}\left(\frac{L_D^2 \lambda_{\text{MIN},i}^2}{4}\right)\right). \tag{48}$$

D. Summary: Analytical Bound on Integrity Risk Accounting for Probability of Correct Association

In this section, we have established an analytical bound on the integrity risk that accounts for the risk of IA. The integrity risk is expressed as follows:

$$\begin{aligned} P(HMI_k) \le 1 - [1 - P(HMI_k|CA_K)] \prod_{j=1}^{k} P(CA_j|CA_{J-1}) \\ + I_{\text{FE,ALLOC},k} \end{aligned} \tag{49}$$

with

$$P(HMI_k|CA_K) = Q\left(\ell/\sigma_k\right) + 1 - Q\left(-\ell/\sigma_k\right) \tag{50}$$

$$P(CA_j|CA_{J-1}) \ge 1 - P\left(q_j^2 \ge \min_{i=1,...,h}\left\{L_{D,j}^2 \lambda_{\text{MIN},i,j}^2/4\right\}\right) \tag{51}$$

Authorized licensed use limited to: to IEEExplore provided by University Libraries | Virginia Tech. Downloaded on August 17,2020 at 19:20:58 UTC from IEEE Xplore. Restrictions apply.

where

k	is an index identifying a time step.
$Q()$	is the tail probability function of the standard normal distribution.
ℓ	is the specified alert limit that defines a hazardous situation.
σ_k	is the standard deviation of the estimation error for the vehicle state of interest.
$I_{\mathrm{REQ},k}$	is the overall integrity risk requirement.
$I_{\mathrm{FE,ALLOC},k}$	is a predefined integrity risk allocation at FE, chosen to be a small fraction of $I_{\mathrm{REQ},k}$.
q_j^2	is a chi-square distributed random variable with a number of DOF that is the sum of the number of measurements and of states at time step j.
$L_{D,j}^2$	can be determined at FE, and is defined in (43), and represents the minimum value of the mean landmark feature separation at time step j.
$\lambda_{\mathrm{MIN},i,j}^2$	can be determined at DA, and is defined in (45) to account for the worst-case projection of the FE's separation vector into the DA's innovation space.

The analytical integrity risk bound in (49)–(51) is implemented, analyzed, and tested in the next two sections.

IV. COVARIANCE ANALYSIS AND DIRECT SIMULATIONS

In this section, two example simulations first analyzed in [33] and [39] are modified to evaluate (49)–(51). The first scenario is an illustrative 2D, two-landmark problem. Simulation results identify cases where the estimation error covariance is not an accurate measure of safety performance. In contrast, the integrity risk bound derived in this paper does account for potential IAs.

A second scenario is simulated under more realistic assumptions, using a multisensor laser/GPS system onboard a vehicle roving across a GPS-denied area, and navigating using static landmarks. This direct simulation scenario helps quantify the significant impact of IA on $P(HMI_k)$, and is used to outline the next steps of this research, i.e., the need for landmark selection and continuity risk evaluation methods.

A. Illustrative Two Landmark Scenario

Figs. 6 and 8 represent a vehicle designated by an upward pointing triangle roving between two landmarks represented by black-shaded circles. The vehicle starts at an initial, known position at point (0, 0) in a local East–North reference frame, and uses measurements from a laser or radar to estimate its position. In this example, vehicle orientation is known (as if given by another sensor, e.g., a perfect inertial navigation system). While roving along the North axis, the vehicle passes by two point-feature landmarks. The actual landmark locations are initially unknown to the navigation system. Landmark locations are simultaneously estimated with vehicle pose in a SLAM-like approach. Simulation parameters are listed in Table I.

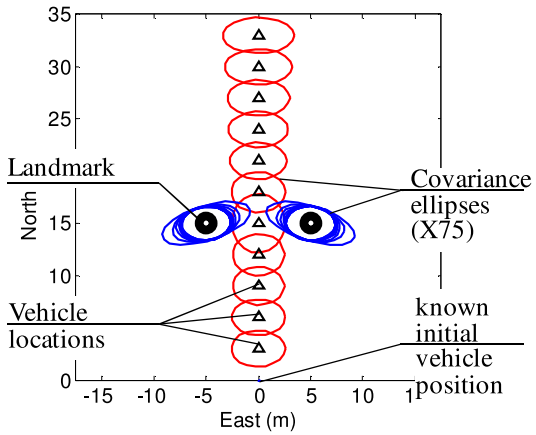

Fig. 6. Covariance analysis for the illustrative two distinguishable landmark scenario.

TABLE I
Simulation Parameters

System Parameters	Values
Standard deviation on raw laser ranging measurement	0.02 m
Standard deviation on raw laser angular measurement	0.5 deg
Laser range Limit	20 m
Laser data sampling interval	0.5 s
Vehicle speed	1 m/s
Alert limit ℓ	0.5 m
Integrity risk allocation for FE, $I_{FE,ALLOC,k}$	10^{-9}

Positioning errors at consecutive sample updates are represented by covariance ellipses in Figs. 6 and 8, for the locations of the vehicle (red ellipses) and landmarks (blue ellipses). These ellipses assume consistently successful FE and DA. We focus on the East–West positioning error, perpendicular to vehicle's straight line trajectory. Cross-track errors are of primary concern for navigation safety, and the cross-track direction is where errors are the largest. A cross-track drift over distance travelled is observed, which is typical of SLAM [14], [43], [44].

1) *Case of Two Distinguishable Landmarks:* In a first case, the actual landmark locations are at $(-5, 15)$ and $(5, 15)$. This relatively large separation makes them easy to distinguish, as suggested by the fact that the blue covariance ellipses for the left and right landmarks do not overlap.

Fig. 7 shows the integrity risk bound labeled $P(HMI_k)$, represented with a red curve, versus northward travel distance as the vehicles passes by the two landmarks. The bound is always larger than $I_{\mathrm{FE,REQ},k} = 10^{-9}$, which is our choice of an example integrity risk requirement allocation. As captured in (49), this $P(HMI_k)$-bound is loose when $P(CA_K) \approx 1$ and $P(HMI_k|CA_K) << 10^{-9}$, which is the case in Fig. 7 for travel distances smaller than 30 m. The $P(HMI_k)$-bound captures the risk involved in FE, and is a

Authorized licensed use limited to: to IEEExplore provided by University Libraries | Virginia Tech. Downloaded on August 17,2020 at 19:20:58 UTC from IEEE Xplore. Restrictions apply.

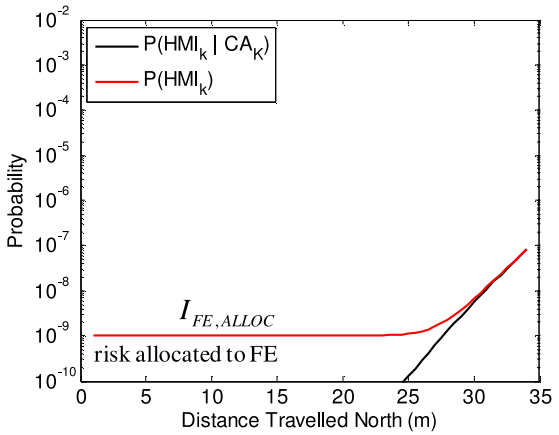

Fig. 7. Integrity risk bound for the illustrative two distinguishable landmark scenario.

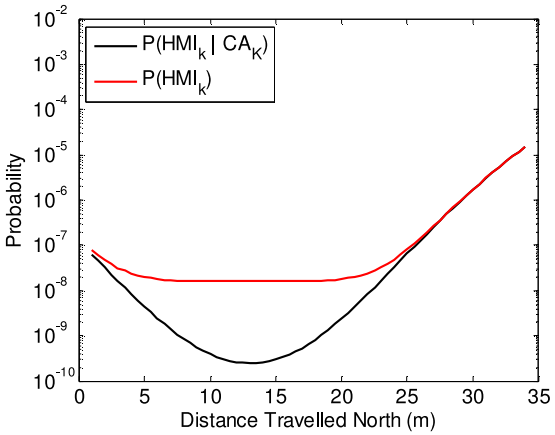

Fig. 9. Integrity risk bound for the illustrative two difficult-to-distinguish landmark scenario.

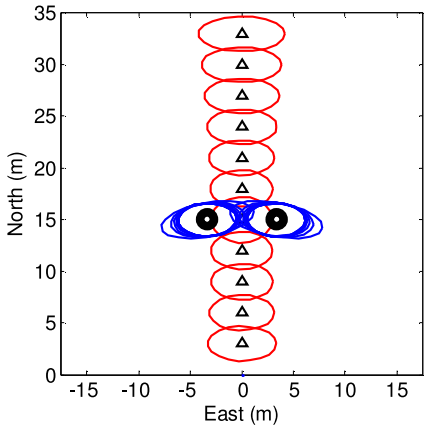

Fig. 8. Covariance analysis for the illustrative two difficult-to-distinguish landmark scenario.

practical bound when trying to achieve an overall example requirement of $I_{\mathrm{REQ},k} = 10^{-7}$.

In parallel, the black curve in Fig. 6 represents the bound on $P(HMI_k|CA_K)$, which is fully determined by the alert limit ℓ and the vehicle positioning covariance. This curve represents a vehicle navigation performance metric often used to evaluate laser-based navigation systems [14], [43], [44]. The black curve converges with our integrity risk bound (red curve) for travel distances larger than 30 m. In this example, the black curve adequately captured the safety risk, because $P(CA_K) \approx 1$. But, the next section will show that it is not always the case.

2) *Case of Two Difficult-to-Distinguish Landmarks:* In this second case, the two landmark locations represented in Fig. 8 are at $(-3.3, 15)$ and $(3.3, 15)$, which makes them more difficult to distinguish than in Fig. 6. The blue covariance ellipses for the two landmarks do overlap with each other.

Fig. 9 displays the $P(HMI_k)$-bound in red, and the $P(HMI_k|CA_K)$-bound in black, versus travel distance. Both curves are orders of magnitude higher than in Fig. 7. This is because the change in geometry between vehicle and landmarks provides less information on vehicle cross-track deviation in Fig. 8 than it did in Fig. 6. This can also be seen with the red ellipses, which are horizontally more elongated in Fig. 8 compared to Fig. 6.

The $P(HMI_k)$-bound shows the impact of possible IAs on the integrity risk. It can be noted that there is a substantial difference between the red and black curves, especially for a travel distance of 15 m where the vehicle is right between landmarks. In this case, the covariance-based $P(HMI_k|CA_K)$-bound is two-orders of magnitude below the $P(HMI_k)$-bound. From a safety perspective, the covariance is a misleading navigation performance metric.

B. Vehicle Roving Through a GPS-Denied Area

This analysis investigates the safety performance of a multisensor GPS/laser system embedded on a vehicle roving through a forest. GPS signals are blocked by the tree canopy, and low-elevation satellite signals do not penetrate under the trees. Tree trunks are used as landmarks by the laser-based SLAM-type algorithm. Additional information on the procedures used to extract point-features and to deal with landmarks coming in and out of view can be found in [39].

The measurement vector $\hat{\mathbf{z}}_k$ in (4) is augmented with GPS code and carrier measurements, and the state vector $\mathbf{x}_k$ is augmented to include an unknown GPS receiver clock bias and initially known carrier phase cycle ambiguities. Time-correlated GPS signals and nonlinear laser data are processed in a unified time-differencing EKF derived in [33] and [39]. The simulation parameter values are listed in Table I, and a standard differential GPS measurement error model is used, which is described in [39]. In this scenario, GPS and lasers essentially relay each other with seamless transitions from open-sky through GPS-denied areas where landmarks modeled as poles with nonzero radii are visible.

Fig. 10 illustrates the interactions between the two sensors, while the GPS/laser-equipped vehicle roves through the GPS-denied area. Three successive snap-shots (a, b, and c) of a direct simulation are presented. On the upper part, azimuth-elevation plots and simulated laser scans present, respectively, the GPS satellite sky blockage within the ob-

Authorized licensed use limited to: to IEEExplore provided by University Libraries | Virginia Tech. Downloaded on August 17,2020 at 19:20:58 UTC from IEEE Xplore. Restrictions apply.

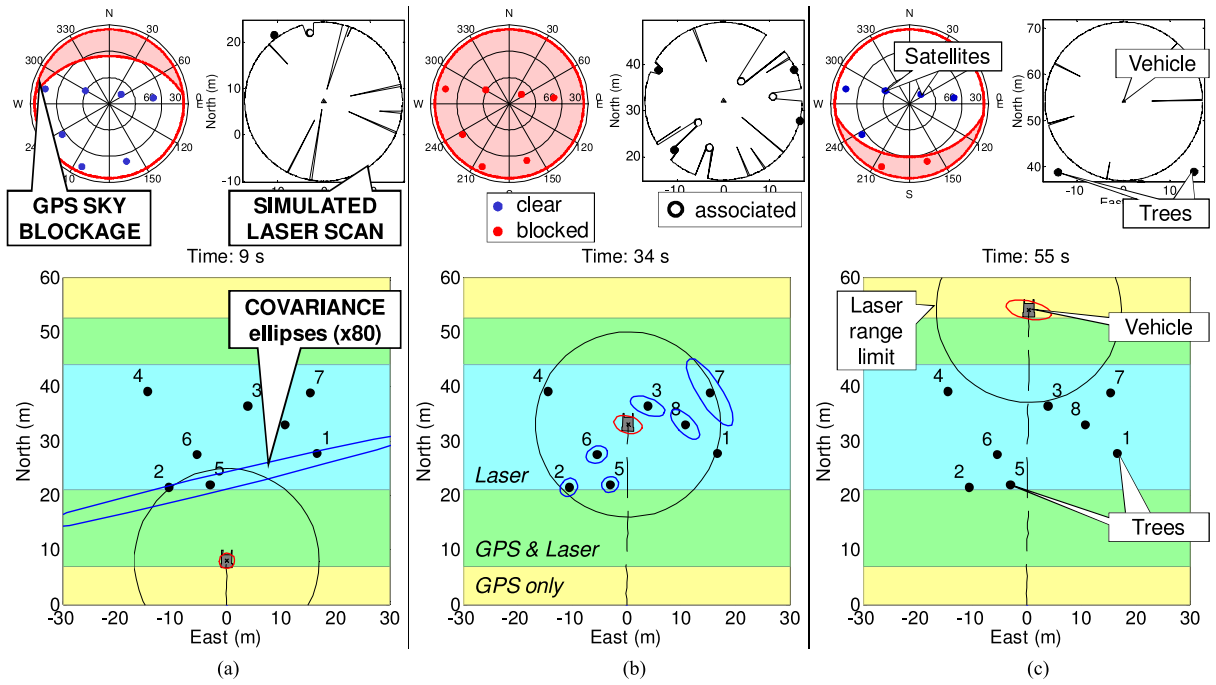

Fig. 10. Direct simulation of the GPS/Laser algorithm in the GPS-denied area scenario. (a) The vehicle started in the GPS-available area (yellow-shaded) and enters the transitional GPS-and-laser-available area (green) where absolute landmark position is being estimated. (b) The vehicle is in the middle of the GPS obstruction and relies on laser/radar-only (blue-shaded area), so that the vehicle pose estimation error increases with travel distance. (c) The vehicle is back into a GPS available area (yellow), and the cross-track positioning drift is stopped.

struction, and the landmarks within range of the laser. The simulated laser measurement error model includes both random uncertainty and large-size impulse-type ranging errors. The result of the estimation process is given on the lower part. Covariance ellipses represent the positioning error on the vehicle and landmarks.

The mission starts with the vehicle operating in a GPS available area (yellow-shaded). The many satellite signals available during this initialization enable accurate estimation of cycle ambiguities, so that the vehicle positioning uncertainty does not exceed a few centimeters. In the next time-steps, as the vehicle crosses the GPS-and-laser available area (green-shaded), and the laser-only area (blue-shaded), seamless variations in covariance are achieved. The yellow–green–blue color code is used consistently in the next figures. A detailed description of this simulation is given in [39].

In this scenario, the likelihood of IA is high. This can be seen on the upper plot in Fig. 11. It shows that the actual cross-track positioning error versus distance travelled is significantly exceeding the corresponding 1σ covariance envelope. It indicates that errors are impacting positioning, which are not captured by the covariance.

This is confirmed on the lower chart of Fig. 11, where the black curve showing the $P(HMI_k|CA_K)$-bound and directly derived from the positioning error covariance stays below 10^{-5}. In contrast, the red curve showing the $P(HMI_k)$-bound indicates much higher risk. The red curve reaches a first plateau of $I_{\text{FE,ALLOC},k}$ due to the risk involved in FE as soon as two landmarks are visible. As discussed in

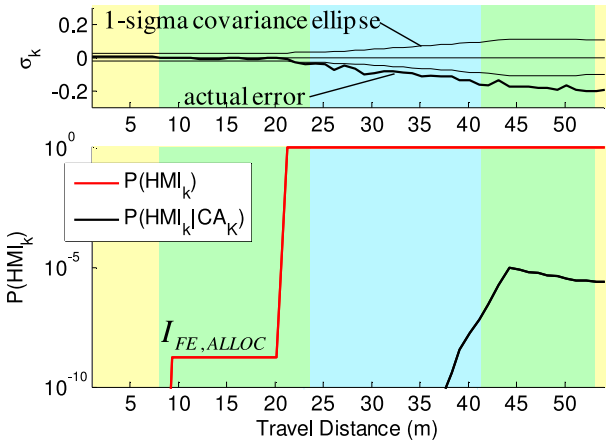

Fig. 11. $P(HMI_k)$-bound for the GPS-denied-area crossing scenario (same color-code as in Fig. 10).

Section IV-A-1), our choice of $I_{\text{FE,ALLOC},k} = 10^{-9}$ is conservative, but it is far below the overall requirement (e.g., assumed to be $I_{\text{REQ},k} = 10^{-7}$) and provides a practical solution to $P(HMI_k)$-bounding when using FE.

The red $P(HMI_k)$-bound curve then suddenly increases to 1, at approximately 21 m of distance travelled. This means that there is not enough information to guarantee that any of the candidate associations is correct. Fig. 12 shows that, at the time step preceding the large increase in predicted integrity risk, landmark 6 is hidden behind landmark 5. Before that point, it was either out of laser range, or hidden behind landmark 5. It will first become visible to

Authorized licensed use limited to: to IEEExplore provided by University Libraries | Virginia Tech. Downloaded on August 17,2020 at 19:20:58 UTC from IEEE Xplore. Restrictions apply.

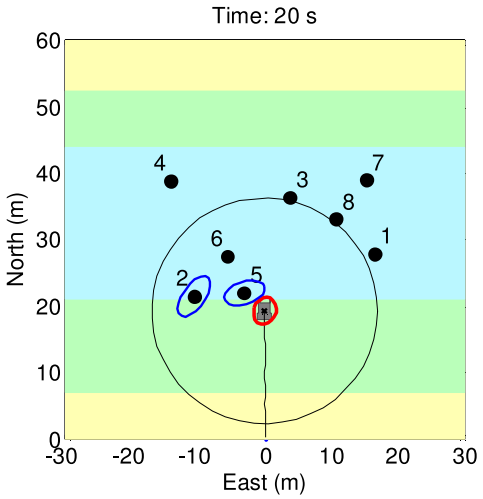

Fig. 12. Time-step preceding the large increase in $P(HMI_k)$-bound in Fig. 10 (same color-code as in Fig. 10).

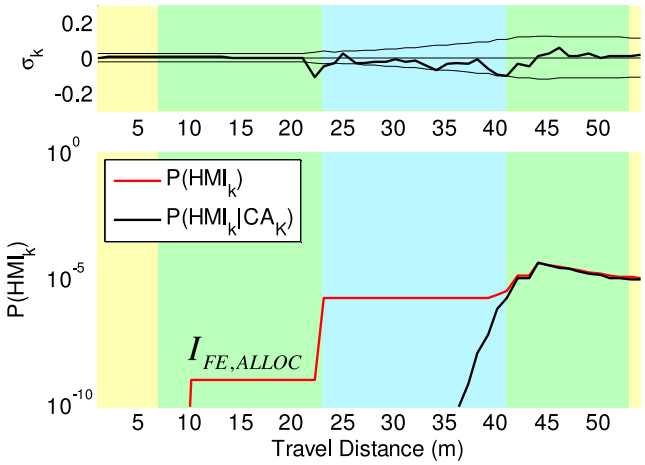

Fig. 13. $P(HMI_k)$-bound for the GPS-denied-area crossing scenario when landmark 6 is not extracted (same color-code as in Fig. 9).

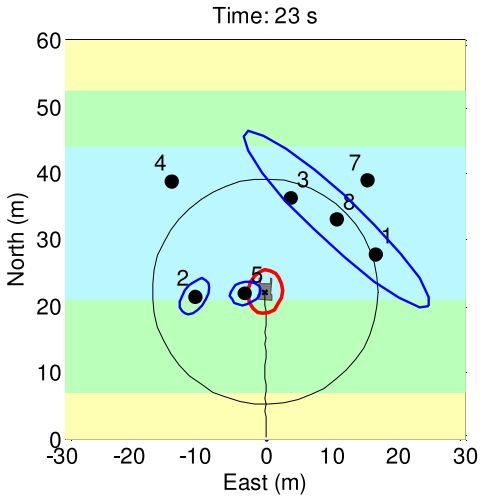

Fig. 14. Time-step preceding the increase in $P(HMI_k)$-bound in Fig. 12 when landmark 6 is not extracted (same color-code as in Fig. 10).

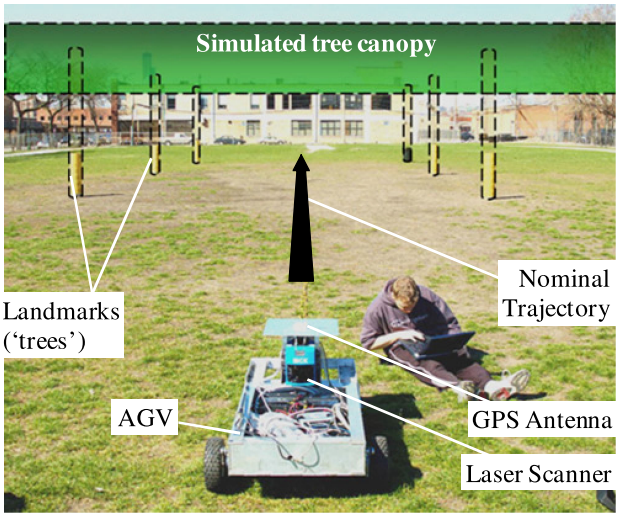

Fig. 15. Experimental setup of a forest-type scenario, where a GPS/Laser-equipped rover is driving by six landmarks (cardboard columns) in a GPS-denied area. GPS is artificially blocked by a simulated tree canopy, and a precise differential GPS solution is used as truth trajectory.

the laser at the next time step, which makes correct measurement association with either landmark 5 or 6 extremely challenging. The $P(HMI_k)$-bound in (49)–(51) provides the means to quantify the impact on integrity risk of such events.

Eliminating landmark 6 reduces occurrences of IAs, as indicated in the upper graph of Fig. 13 where the positioning error now fits the covariance envelope. Risk reduction is also observed in the lower chart, where the $P(HMI_k)$-bound does not exceed 10^{-5} (versus 1 in Fig. 11). The red curve in Fig. 13 still exhibits a sudden increase at about 23 m of travel distance. This is because, as shown in Fig. 14, landmark 2 that was temporarily hidden behind landmark 5 will suddenly become visible again. The resulting risk of incorrectly associating measurements with landmarks 2 or 5 is quantified as being about 10^{-6}.

This risk can be further reduced by eliminating even more landmarks using a feature selection method. However, this approach has its limits because if landmarks keep being removed, there will eventually not be enough extracted measurements to provide *continuous* positioning.

This section has pointed out a key tradeoff in laser-based navigation safety: on the one hand, a large number of extracted measurements ensure continuous positioning, but on the other hand, it lowers navigation integrity because it increases the risk of IAs. Future work will investigate ways to design landmark selection algorithms and to quantify continuity risk.

V. PRELIMINARY EXPERIMENTAL TESTING

Preliminary experimental testing of the method derived in Sections II and III is carried out using data collected in a structured environment shown in Fig. 15. Static simple-shaped landmarks are located at locations sparse enough to ensure successful outcomes for FE and DA. Because

Authorized licensed use limited to: to IEEExplore provided by University Libraries | Virginia Tech. Downloaded on August 17,2020 at 19:20:58 UTC from IEEE Xplore. Restrictions apply.

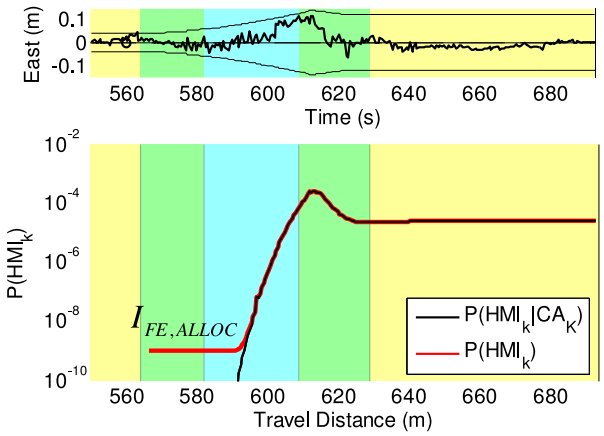

Fig. 16. Integrity risk bounds versus travel distance for the preliminary experimental data set capturing a forest-type scenario (same color-code as in Fig. 10).

the results presented here are free of IAs, they describe the estimation process, and $P(HMI_k)$ is expected to match $P(HMI_k|CA_K)$. Practical implementation of the proposed method in more realistic HAV environments requires landmark selection and unwanted obstacle detection [38], which are not addressed in this paper.

Measurements from carrier phase differential GPS (CPDGPS) as well as laser scanners are synchronized and recorded. In order to obtain a full 360 °C laser scan, two 180 °C laser scanners are assembled back-to-back. The laser scanners have a specified 15–80 m range limit, a 0.5 °C angular resolution, a 5 Hz update rate, and a ranging accuracy of 1–5 cm (1σ) [45]. The GPS antenna is mounted on top of the front laser. The lever-arm distance between the two lasers is included in the measurement model.

The two lasers and the GPS antenna are mounted on rover also carrying the GPS receiver and data link. An embedded computer onboard the vehicle records all measurements including the raw GPS data from the reference station transmitted via wireless spread-spectrum data-link. Truth vehicle trajectory and landmark locations are obtained using a fixed CPDGPS solution.

In this forest-type scenario, landmarks are tree-trunks reproduced using five cardboard columns and one dark plastic garbage can. Because there is actually no physical obstruction to the sky, satellite masking for the GPS/laser integration system is performed artificially as illustrated in Fig. 15: an artificially simulated tree canopy blocks high-elevation satellite signals; low-elevation GPS observations are not used either inside the obstruction.

As mentioned in the first paragraph of this section, the landmark geometry in this experiment is such that the risk of IA is extremely small. This is confirmed on the upper chart in Fig. 16 where the actual error (thick line) fits the covariance envelope (thin line) throughout the test. The lower graph also shows that the $P(HMI_k)$-bound matches the $P(HMI_k|CA_K)$-bound, except between 565 and 600 m of travel distance where the predefined integrity risk allocation for FE is the dominant term in the $P(HMI_k)$-bound.

This test shows that the method derived in this paper can be implemented using actual data from a multisensor GPS/laser system, and that the analytical integrity risk bound is tight when the risk of IA is small.

VI. CONCLUSION

This paper presents a new approach to ensure the safety of laser-based navigation using FE and DA by quantifying the integrity risk.

An analytical integrity risk bound is established, which accounts for all possible ways FE and DA can fail. First, at FE, a minimum normalized separation metric is derived, which evaluates, in a statistically quantifiable manner, how distinguishable landmarks are. Then, at DA, an innovation-based nearest-neighbor association criterion is employed to evaluate the risk of all potential IAs, at each time step in the iterative vehicle pose estimation process.

Performance evaluations are carried out by covariance analysis and direct simulation, showing that the positioning error covariance is a misleading safety performance metric. Cases are shown where the contributions of IAs to integrity risk far surpass that of nominal errors accounted for in the positioning error covariance. In addition, a key tradeoff in FE and DA is pointed out: more extracted measurements ensure *continuous* positioning, but reduce integrity because of the increased risk of IA. The next step of this research will aim at quantifying the continuity risk of FE and DA, which is an essential aspect of navigation safety.

Finally, preliminary experimental testing was carried out using a multisensor GPS/laser system onboard a vehicle roving in a structured environment. It showed that the integrity risk evaluation method can be implemented with real data. Future testing will be performed in a more realistic passenger vehicle operating environment using FE and selection methods that are more advanced than the ones implemented in this paper.

APPENDIX

This appendix shows that: $\lambda_{\mathrm{MAX},i} = 1$ and $\lambda_{\mathrm{MAX},0} = 1$, where $\lambda^2_{\mathrm{MAX},i}$ and $\lambda^2_{\mathrm{MAX},0}$, respectively, are the maximum eigenvalues of $\mathbf{R}^{1/2}(\mathbf{M}_i\mathbf{Y}_i^{-1}\mathbf{M}_i^T)\mathbf{R}^{1/2}$ and $\mathbf{R}^{1/2}(\mathbf{M}_0\mathbf{Y}_0^{-1}\mathbf{M}_0^T)\mathbf{R}^{1/2}$.

The following derivation shows that $\mathbf{R}^{1/2}(\mathbf{M}_i\mathbf{Y}_i^{-1}\mathbf{M}_i^T)\mathbf{R}^{1/2}$, which is symmetric (obvious), is also idempotent [46] for $i = 0, ..., h$. By definitions of $\mathbf{M}_i$ and $\mathbf{R}$ in (29) and (30), the following equations can be written to show idempotence:

$$\begin{aligned}
&\mathbf{R}^{1/2}(\mathbf{M}_i\mathbf{Y}_i^{-1}\mathbf{M}_i^T)\mathbf{R}^{1/2}\mathbf{R}^{1/2}(\mathbf{M}_i\mathbf{Y}_i^{-1}\mathbf{M}_i^T)\mathbf{R}^{1/2}\\
&= \mathbf{R}^{1/2}\mathbf{M}_i\mathbf{Y}_i^{-1}\begin{bmatrix}\mathbf{I} & -\mathbf{A}_i\mathbf{H}\end{bmatrix}\begin{bmatrix}\mathbf{V} & \mathbf{0}\\ \mathbf{0} & \bar{\mathbf{P}}\end{bmatrix}\begin{bmatrix}\mathbf{I}\\ -\mathbf{H}_i^T\mathbf{A}_i^T\end{bmatrix}\mathbf{Y}_i^{-1}\mathbf{M}_i^T\mathbf{R}^{1/2}\\
&= \mathbf{R}^{1/2}\mathbf{M}_i\mathbf{Y}_i^{-1}(\mathbf{V} + \mathbf{A}_i\mathbf{H}_i\bar{\mathbf{P}}\mathbf{H}_i^T\mathbf{A}_i^T)\mathbf{Y}_i^{-1}\mathbf{M}_i^T\mathbf{R}^{1/2}\\
&= \mathbf{R}^{1/2}\mathbf{M}_i\mathbf{Y}_i^{-1}\mathbf{M}_i^T\mathbf{R}^{1/2}
\end{aligned}$$

where the last equation is obtained by definition of $\mathbf{Y}_i$ in (26). The above derivation shows that $\mathbf{R}^{1/2}\mathbf{M}_i\mathbf{Y}_i^{-1}\mathbf{M}_i^T\mathbf{R}^{1/2}$ is idempotent for $i = 0, ..., h$.

Authorized licensed use limited to: to IEEExplore provided by University Libraries | Virginia Tech. Downloaded on August 17,2020 at 19:20:58 UTC from IEEE Xplore. Restrictions apply.

Thus, the eigenvalues of the rank-deficient matrix $\mathbf{R}^{1/2}(\mathbf{M}_i\mathbf{Y}_i^{-1}\mathbf{M}_i^T)\mathbf{R}^{1/2}$ are ones and zeros, and the maximum eigenvalue $\lambda^2_{\mathrm{MAX},i}$ (and $\lambda^2_{\mathrm{MAX},0}$ for $i = 0$) is equal to one. It follows that: $(\lambda_{\mathrm{MAX},i} + \lambda_{\mathrm{MAX},0})^2 = 4$.

ACKNOWLEDGMENT

The opinions expressed in this paper do not necessarily represent those of any other organization or person.

REFERENCES

[1] Y. Bar-Shalom and T. E. Fortmann
Tracking and data association
In *Mathematics in Science and Engineering*, vol. 179. San Diego, CA, USA: Academic Press, 1988.

[2] T. Bailey
Mobile robot localisation and mapping in extensive outdoor environments
Ph.D. dissertation, Univ. of Sydney, Sydney, Australia, 2002.

[3] T. Bailey and J. Nieto
Scan-SLAM: Recursive mapping and localisation with arbitrary-shaped landmarks
In *Proc. Workshop of IEEE Robot.: Sci. Syst.*, Zurich, Switzerland, 2008, pp. 1–12.

[4] A. J. Cooper
A comparison of data association techniques for simultaneous localization and mapping
M.S. Thesis, Massachussetts Inst. Technol., Cambridge, MA, USA, 2005.

[5] S. T. Pfister, K. L. Kriechbaum, S. I. Roumeliotis, and J. W. Burdick
Weighted range sensor matching algorithms for mobile robot displacement estimation
In *Proc IEEE Int. Conf. Robot. Autom.*, 2002, pp. 1667–1674.

[6] S. T. Pfister, S. I. Roumeliotis, and J. W. Burdick
Weighted line fitting algorithms for mobile robot map building and efficient data representation robotics and automation
In *Proc. IEEE Int. Conf. Robot. Autom.*, 2003, pp. 1304–1311.

[7] I. T. Ruiz, Y. Petillot, D. M. Lane, and C. Salson
Feature extraction and data association for AUV concurrent mapping and localisation
In *Proc. IEEE Int. Conf. Robot. Autom.*, 2001, pp. 2785–2790.

[8] S. Thrun
Robotic mapping: A survey
In *Exploring Artificial Intelligence in the New Millenium*, G. Lakemeyer and B. Nebel, Eds. San Francisco, CA, USA: Morgan Kaufmann, Feb. 2002.

[9] S. Thrun, W. Burgard, and D. Fox
A probabilistic approach to concurrent mapping and localization for mobile robots
Mach. Learn. Auton. Robots, vol. 31, no. 5, pp. 1–25, 1998.

[10] S. Thrun, W. Burgard, and D. Fox
"A real-time algorithm formobile robot mappingwith applications to multi-robot and 3D mapping
In *Proc. IEEE Int. Conf. Robot. Autom.*, San Francisco, CA, USA, 2000, pp. 321–328

[11] V. Nguyen, A. Martinelli, N. Tomatis, and R. Siegwart
A comparison of line extraction algorithms using 2D laser rangefinder for indoor mobile robotics
In *Proc. IEEE/RSJ Int. Conf. Intell. Robots Syst.*, 2005, pp. 1929–1934.

[12] P. Nunez, R. Vazquez-Martin, J. C. del Toro, and A. Bandera
Feature extraction from laser scan data based on curvature estimation for mobile robotics
In *Proc. IEEE Int. Conf. Robot. Autom.*, 2006, pp. 1167–1172.

[13] Y. Li and E. B. Olson
A general purpose feature extractor for light detection and ranging data
Sensors, vol. 10, no. 11, pp. 10356–10375, 2010.

[14] R. Madhavan, H. Durrant-Whyte, and G. Dissanayake
Natural landmark-based autonomous navigation using curvature scale space
In *Proc. IEEE Int. Conf. Robot. Autom.*, 2002, pp. 3936–3941.

[15] D. Maksarov and H. Durrant-Whyte
Mobile vehicle navigation in unknown environments: A multiple hypothesis approach
IEE Control Theory Appl., vol. 142, no. 4, pp. 385–400, 1995.

[16] Waymo We've reached 3 million miles of self-driving on public roads! That's 1 million miles in just 7 months
Waymo on Tweeter, May 2017. [Online]. Available: https://twitter.com/waymo/status/862077212740145152?lang = en

[17] S. Abuelsamid
Adding some statistical perspective to tesla autopilot safety claims *Forbes*, 2016.
[Online]. Available: http://www.forbes.com/sites/samabuelsamid/2016/07/05/adding-some-statistical-perspective-to-tesla-autopilot-safety-claims/#49f09e0c2f8f

[18] The Tesla Team A tragic loss 2016.
[Online]. Available: https://www.tesla.com/blog/tragic-loss

[19] National Highway Traffic Safety Administration Fatality analysis reporting system
Nat. Highway Traffic and Safety Admin, Washington, DC, USA, Tech. Rep. DOT HS 812 246, 2014.

[20] National Highway Traffic Safety Administration National motor vehicle crash causation survey: Report to congress
U.S. Dept. Transp., VA, USA, Tech. Rep. DOT HS 811 059, 2008.

[21] N. Kalra and S. Paddock
Driving to safety: How many miles of driving would it take to demonstrate autonomous vehicle reliability
Rand Corp., vol. 94, pp. 182–193, 2016.

[22] National Highway Traffic and Safety Administration Federal automated vehicles policy: Accelerating the next revolution in roadway safety 2016.
[Online]. Available: https://www.transportation.gov/AV/federal-automated-vehicles-policy-september-2016

[23] RTCA Special Committee 159, *Minimum Aviation System Performance Standards for the Local Area Augmentation System*
RTCA/DO-245 Standard, 2004, Appendix D.

[24] Y. C. Lee
Analysis of range and position comparison methods as a means to provide GPS integrity in the user receiver
In *Proc. 42nd Annu. Meet. Inst. Navig.*, Seattle, WA, USA, 1986, pp. 1–4.

[25] B. W. Parkinson and P. Axelrad
Autonomous GPS integrity monitoring using the pseudorange residual
NAVIGATION, vol. 35, no. 2, 1988, pp. 225–274.

[26] RTCA Special Committee 159, *Minimum Operational Performance Standards for Global Positioning System/Wide Area Augmentation System Airborne Equipment*
RTCA/DO-229C Standard, 2001, pp. 1–21.

[27] J. Leonard and H. Durrant-Whyte
Directed Sonar Sensing for Mobile Robot Navigation, Cambridge, MA, USA: Kluwer, 1992, pp. 129–138.

[28] S. B. Williams, G. Dissanayake, and H. Durrant-Whyte
An efficient approach to the simultaneous localisation and mapping problem
In *Proc. IEEE Int. Conf. Robot. Autom.*, 2002, pp. 406–411.

[29] F. Lu and E. Milios
Globally consistent range scan alignment for environment mapping
Auton. Robots, vol. 4, pp. 333–349, 1997.

[30] T. Röfer
Using histogram correlation to create consistent laser scan maps
In *Proc. IEEE Int. Conf. Intell. Robots Syst.*, Lausanne, Switzerland, 2002, pp. 625–630.

Authorized licensed use limited to: to IEEExplore provided by University Libraries | Virginia Tech. Downloaded on August 17,2020 at 19:20:58 UTC from IEEE Xplore. Restrictions apply.

[31] A. Diosi and L. Kleeman
Laser scan matching in polar coordinates with application to SLAM
In *Proc. IEEE/RSJ Int. Conf. Intell. Robots Syst.*, 2005, pp. 3317–3322.

[32] O. Bengtsson and A. J. Baerveldt
Robot localization based on scan-matching-estimating the covariance matrix for the IDC algorithm
Robot. Auton. Syst., vol. 44, pp. 29–40, 2003.

[33] M. Joerger and B. Pervan
Measurement-level integration of carrier-phase GPS and laser-scanner for outdoor ground vehicle navigation
ASME J. Dyn. Syst. Meas. Control, vol. 131, pp. 021004-1–021004-11, 2009.

[34] Y. Bar-Shalom, F. Daum, and J. Huang
The probabilistic data association filter
IEEE Control Syst. Mag., vol. 29, no. 6, pp. 82–100, Dec. 2009.

[35] F. C. Chan, M. Joerger, S. Khanafseh, and B. Pervan
Bayesian fault-tolerant position estimator and integrity risk bound for GNSS navigation
J. Navig. Royal Inst. Navig., vol. 67, pp. 753–775, 2014, doi:10.1017/S0373463314000241.

[36] J. Areta, Y. Bar-Shalom, and R. Rothrock
Misassociation probability in M2TA and T2TA
J. Adv. Inf. Fusion, vol. 2, no. 2, pp. 113–127, 2007.

[37] G. Duenas Arana, M. Joerger, and M. Spenko
Minimizing integrity risk via landmark selection in mobile robot localization
In *Proc. IEEE Trans. Robot.*, 2018.

[38] M. Joerger, G. Duenas Arana, M. Spenko, and B. Pervan
Landmark data selection and unmapped obstacle detection in lidar-based navigation
In *Proc.Inst. Navig. Global Navig. Satellite Syst.*, Portland, OR, 2017, pp. 1886–1903.

[39] M. Joerger
Carrier phase GPS augmentation using laser scanners and using low earth orbiting satellites
Illinois Inst. Technol., Ph.D. dissertation, Chicago, IL, USA, 2009.

[40] B. DeCleene
Defining pseudorange integrity – Overbounding
In *Proc. Inst. Navig. Global Positioning Syst.*, Salt Lake City, UT, USA, 2000, pp. 1916–1924.

[41] J. Rife, S. Pullen, P. Enge, and B. Pervan
Paired overbounding for nonideal LAAS and WAAS error distributions
IEEE Trans. Aerosp. Electron. Syst., vol. 42, no. 4, pp. 1386–1395, Oct. 2006.

[42] M. Joerger, M. Jamoom, M. Spenko, and B. Pervan
Integrity of laser-based feature extraction and data association
In *Proc. IEEE/Inst. Navig. Position, Location Navig. Symp.*, Savannah, GA, 2016, pp. 557–571.

[43] F. Bayoud
Vision-aided inertial navigation using a geomatics approach
In *Proc. Inst. Navig. Global Navig. Satellite Syst.*, Long Beach, CA, USA, 2005, pp. 2485–2493.

[44] G. Dissanayake, P. Newman, S. Clark, H. Durrant-Whyte, and M. Csorba
A solution to the simultaneous localization and map building (SLAM) problem
IEEE Trans. Robot. Autom., vol. 17, no. 3, pp. 229–241, Jun. 2001.

[45] C. Ye and J. Borenstein
Characterization of a 2-D laser scanner for mobile robot obstacle negotiation
In *Proc. IEEE Int. Conf. Robot. Autom.*, May 2002, pp. 2512–2518.

[46] A. Jeffrey
Advanced Engineering Mathematics, Harcourt: Academic, 2002.

Dr. Mathieu Joerger (M'14–SM'18) received the 'Diplôme d'Ingenieur' (Master degree) in mechatronics from the National Institute of Applied Sciences, Strasbourg, France, the M.S. and Ph.D. degree in mechanical and aerospace engineering from the Illinois Institute of Technology, Chicago, IL, USA.

He is currently an Assistant Professor of Aerospace and Mechanical Engineering with the University of Arizona, Tucson, AZ , USA, working on multisensor integration, on sequential fault-detection for multiconstellation navigation systems, and on relative and differential receiver autonomous integrity monitoring for shipboard landing of military aircraft.

Dr. Joerger was the recipient of the Institute of Navigation Bradford Parkinson Award in 2009, and ION Early Achievement Award in 2014.

Authorized licensed use limited to: to IEEExplore provided by University Libraries | Virginia Tech. Downloaded on August 17,2020 at 19:20:58 UTC from IEEE Xplore. Restrictions apply.

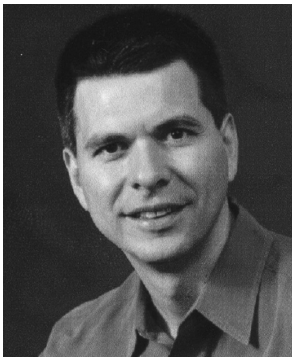

Dr. Boris Pervan (SM'15) received the B.S. degree in aerospace engineering from the University of Notre Dame, Notre Dame, IN, USA, the M.S. degree in aeronautics from the California Institute of Technology, Pasadena, CA, USA, and the Ph.D. degree in aeronautics and astronautics from Stanford University, Stanford, CA, USA.

He is currently a Professor of Mechanical and Aerospace Engineering with the Illinois Institute of Technology, Chicago, IL, USA, where he conducts research on advanced navigation systems. Prior to joining the faculty at IIT, he was a Spacecraft Mission Analyst with Hughes Aircraft Company (now Boeing) and a Postdoctoral Research Associate with Stanford University, Stanford, CA, USA.

Dr. Pervan is an Associate Fellow of the American Institute of Aeronautics and Astronautics, a Fellow of the Institute of Navigation (ION), and Editor-in-Chief of the ION journal Navigation. He was the recipient of the IIT Sigma Xi Excellence in University Research Award (2011, 2002), Ralph Barnett Mechanical and Aerospace Dept. Outstanding Teaching Award (2009, 2002), Mechanical and Aerospace Dept. Excellence in Research Award (2007), University Excellence in Teaching Award (2005), IEEE Aerospace and Electronic Systems Society M. Barry Carlton Award (1999), RTCA William E. Jackson Award (1996), Guggenheim Fellowship (Caltech 1987), and Albert J. Zahm Prize in Aeronautics (Notre Dame 1986).

Authorized licensed use limited to: to IEEExplore provided by University Libraries | Virginia Tech. Downloaded on August 17,2020 at 19:20:58 UTC from IEEE Xplore. Restrictions apply.